



Onboard Target Searching Strategy During Lost in Space Situations in Angles-Only Navigation Active Space Debris Removal

Yue You^{1,2} · Hua Wang²

Received: 7 June 2016 / Revised: 12 February 2019 / Accepted: 25 February 2019 / Published online: 1 April 2019
© The Korean Society for Aeronautical & Space Sciences 2019

Abstract

During the transition from ground-based to on-board relative navigation, active space debris removal faces the so-called lost in space problem where the target's orbital parameters are known to a limited degree making its detection and identification among the other visible objects challenging. Being non-cooperative, the target is also assumed to be non-responsive to communication methods. Seven target search strategies are developed and evaluated using Monte-Carlo analysis. It is shown that one of the proposed methods, stepping-sweeping, can insure detection of the target within several minutes with a 99.9% success rate using either a single optical/infra-red camera payload. A sensitivity analysis was conducted on both the camera parameters and the detection success condition and reveals that this target search strategy is robust against initial position uncertainties. It is also applicable to all the common relative trajectories for orbital proximity operations. The developed tool can also be used for sensor parameters as well as search strategy key parameters selection.

Keywords Onboard target searching · Lost in space · Angles-only navigation · Linear covariance analysis · Active debris removal

1 Introduction

Space debris in Earth's orbit could collide with active artificial spacecraft, which is threatening human space assets. While some large pieces of debris are tracked by ground radar, the large majority of pieces remain invisible [1]. After the collision between Iridium 33 and Kosmos-2251, space debris mitigation has become an international problem [2]; 5–10 of the currently existing large debris should be removed each year by 2020 [3]. Among the solutions being tested for eliminating dangerous debris orbiting the Earth, CleanSpace One [4] (CSO) of EPFL is one of the most representative. Built using Commercial Off-The-Shelf (COTS) components, CSO's aim is to autonomously intercept, capture and de-orbit EPFL's own "Swiss Cube", a 1-kg satellite launched in 2009. The disruptive technologies developed

and demonstrated through this project will form the baseline for the upcoming active debris removal (ADR) efforts and also could serve for other on-orbit servicing and inspection mission.

Satellites in the sub-50 kg range allow keeping demonstration missions such as CSO low-cost relative large/full-fledged mission. They, however, have limited payload capabilities. Angles-only relative navigation (AON) provides a low-volume/mass, power saving, and low-cost solution for such micro-/nano-satellite missions and is currently an active area of research [5–16]. A series of vision-based experimental spacecraft was launched in an attempt to develop rendezvous and proximity operations technology that would be more appropriate for small satellite, such as the eXperimental Satellite System-11 (XSS-11, April 2005) [17, 18], Demonstration of Autonomous Rendezvous Technology (DART, April 2005) [19], and Orbital Express [20, 21] (OE, March 2007).

A more recent example is the Prototype Research Instruments and Space Mission Technology Advancement [22] (PRISMA) in-orbit tested, which was launched in June 15, 2010 to demonstrate strategies and technologies for formation flying and rendezvous. The mission qualifies a series of sensor including GPS, vision-based sensors (VBS), and

✉ Yue You
youyue_nudt@126.com

¹ Naval Research Academy, Beijing 100161,
People's Republic of China

² College of Aerospace Science and Engineering, National
University of Defense Technology, Changsha 410073,
Hunan, People's Republic of China

radio frequency relative sensor (RF). Several in-orbit AON experiments were conducted together by OHB Sweden [23], DLR [10], and CNES [24] during the PRISMA mission [25], between the active Chaser Mango and a cooperative target Tango, which is equipped with a LED-based cooperative system; real position uncertainty and non-cooperative target were imitated.

During the far-to-medium phase transition, i.e. the hand-over between on-ground sensors to on-board sensors, the chaser will have to resolve the lost-in-space situation which results from the high (relative) inaccuracy of the ground-provided information such as Two-Line Elements (TLE). The chaser will have to find, positively identify and determine the orbital parameters of the target using non-cooperative methods. The AON approach relies on information provided by the optical or infrared cameras which we refer to as Vision-Based Sensors (VBS).

In PRISMA, the VBS designed by DTU enables optical navigation in both non-cooperative mode and cooperative mode [26]. The VBS whose design is derived from the μ ASC star tracker have been specifically tailored to achieve two complementary navigation purposes: long-distance detection and tracking of a moving target (far-range VBS), and relative position/attitude estimation of a cooperative target (close-range VBS). In far range mode, the camera processing unit is capable of discrimination luminous objects that do not belong to the star catalog and that can be consistently detected as potential orbital targets after a few acquisition cycles given their apparent motion. During the extended phase of PRISMA, Advanced Rendezvous Demonstration using Global Positioning System and Optical Navigation (ARGON, April 2012) has been conducted by DLR; a man-in-the-loop handover from NORAD TLES to angles-only navigation at large separation (30 km) during which GPS was used for the chaser's routine orbit determination and maneuver calibration. During each ground contact a sequence of pictures taken by VBS was downloaded from the chaser, the single batches corresponding to nearly one orbit of data sampled about every 30 s. Image processing (IMP) for target detection [10] was carried out on-ground; this man-in-the-loop target detection strategy is effective, yielding a 83.4–99.6% detection rate¹. The main limitation in this case, however, is the reliance on down-linking of video streams and human validation making the approach non-real-time/offline.

In the system functions, the onboard target searching technique is similar as the pointing, acquisition, and tracking (PAT) of inter satellite optical communication [27–30]. As a result, some of the more mature technologies in the inter

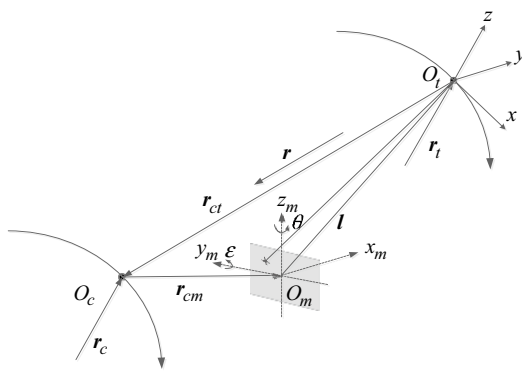
satellite optical communication can be used for reference to speed up the research progress [31]. Many scholars have used the PAT technology of satellite optical communication for reference and explored the influence of the disturbance caused by the satellite platform in the satellite laser communication. And as in the United States STRV-2 and ESA's SILEX in-space experiment [32], they both employed the bidirectional acquisition mode, this mode is not feasible for uncooperative situation, such as debris removal detection. But due to technical confidentiality and other reasons, only the basic parameters of the system and some experimental results are released.

This paper aims at developing an autonomous, robust, and reliable onboard solution for “lost in space” target detection. Stefan [33] suggests in his master thesis that making use of relative motion between chaser and target while scanning increases the likelihood of orbital parameter determination. However, no particular strategy is suggested. In the present paper, we make use of the target's TLE tracking uncertainty information (any debris whose cross-section is roughly equal or above 10 cm can be tracked by NORAD) to initialize the error estimate on the target's position and employ relative orbital dynamics to propagate the evolution of this error ellipsoid. Various scanning strategies are then evaluated.

In preliminary studies, the use of an optical camera is recommended for long- and medium-range navigation; typical hardware includes the Dragon Eye from Advanced Scientific Concept Inc. that offers a 128×128 resolution over a 45° FOV and a demonstrated detection range of about 10 km. The detection is, therefore, expected to become more difficult because the projection of the target's position uncertainty ellipsoid on the sensor's focal plane is much larger. In the context of the Clohessy–Wiltshire dynamics, a tool for AON is developed based on iterative estimation of the target's position error covariance; and seven target searching strategies are explored. In order to conduct the strategy performance comparison as well as sensitivity analysis, a STK/HPOP-embedded Monte Carlo shooting (MCS) tool is built. The developed target searching strategy is robust against target position uncertainty and is applicable to all the common relative trajectories in orbital proximity operations. The selection of camera parameters and minimum searching duration can be constrained as well.

The formulation of the AON-based target search is presented in Sect. 2 and its general solution based on STK/HPOP embedded MCS tool is presented in Sect. 3. The AON closed-loop linear covariance analysis tool and covariance analysis-based target searching strategies are developed and compared in Sect. 4. The strategy performance sensitivity analysis both on the camera parameter and the mission condition is conducted in Sect. 5. Conclusions are presented in Sect. 6.

¹ An excerpt can be seen here: <https://www.youtube.com/watch?v=fbrvJBvndn4>.

**Fig. 1** Relative observation geometry

2 Problem Formulation

Figure 1 illustrates the reference frames and vector quantities associated with the lost in space target searching problem [34–37]. The origin of a rotating LVLH reference frame ($O_t - xyz$) is colocated with the debris c.m. The relative position and velocity of the chaser c.m. with respect to the target c.m. in the LVLH coordinates are denoted by \mathbf{r} and \mathbf{v} , respectively, and the relative state is defined as $\mathbf{x} = [\mathbf{r}, \mathbf{v}]^T$.

The in-orbit relative motion equations for near-circular orbits are the well-known Hill equations whose homogeneous solution is known as the Clohessy–Wiltshire (CW) equations [38]. These solutions can be written in discrete form for impulsive input $\Delta\mathbf{v}_k$ as follows:

$$\mathbf{x}_t = \Phi(t, t_0)\mathbf{x}_0 + \delta(t_k) \begin{bmatrix} \mathbf{0}_{3 \times 1} \\ \Delta\mathbf{v}_k \end{bmatrix}, \quad (1)$$

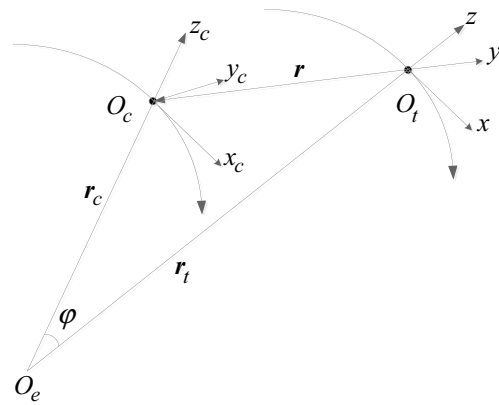
where \mathbf{x}_t , \mathbf{x}_0 are the states at t and t_0 ; $\Delta\mathbf{v}_k$ is the impulsive maneuver vector at t_k , $\delta(t_k)$ is the Dirac function, and $\Phi(t, t_0)$ is the state transfer matrix, given as follows:

$$\Phi(t, t_0) = \begin{bmatrix} \Phi_{rr}(t, t_0) & \Phi_{rv}(t, t_0) \\ \Phi_{vr}(t, t_0) & \Phi_{vv}(t, t_0) \end{bmatrix}. \quad (2)$$

For specific expression of state transfer matrix, $\Phi(t, t_0)$, please refer to Eq. (2.20) in [15].

The camera measure frame ($O_m - x_m y_m z_m$) is assumed to be aligned with the focal plane of the camera, and its orientation with respect to the chaser body frame is assumed to be known and constant. The pixel location of the debris c.m. is used to form a line of sight (LOS) vector from the debris c.m. to the camera, expressed in the camera frame and denoted by $\mathbf{l} = [x_m \ y_m \ z_m]^T$. The angles/bearings-only measure equation provides the measure angles to the debris, can be written explicitly as follows:

$$\mathbf{Z}_{\text{CAM}} = \begin{bmatrix} \epsilon \\ \theta \end{bmatrix} = \mathbf{h}(\mathbf{l}) = \begin{bmatrix} \arctan(z_m/x_m) \\ \arctan(y_m/\sqrt{x_m^2 + z_m^2}) \end{bmatrix}, \quad (3)$$

**Fig. 2** Transition between target's LVLH frame and chaser's LVLH frame

where ϵ, θ are the elevation and azimuth measure angles.

During autonomous relative navigation, the range between chaser and target, r , is negligible compared with radius of the target circular motion, r_t . The target LVLH and chaser LVLH are approximately parallel in inertial space, shown as Fig. 2.

By definition, φ is the rotation angle between two LVLH frames and approximately achieved as follows:

$$\varphi \approx \frac{r}{r_t}. \quad (4)$$

Take the micro-satellite SwissCube for example; it circles the Earth on a 700 km-height circular orbit, when a chaser is 10 km away from it, the angle $\varphi \approx 0.0014 \text{ rad} = 0.0802^\circ$, which is negligible.

At any time, t , the transition from target LVLH to camera measure frame can be calculated using chaser's inertial position, \mathbf{r}_c , inertial velocity, \mathbf{v}_c , and inertial attitude; as result, the observation angles can be calculated using chaser's relative position, $\mathbf{r} = [x \ y \ z]^T$, as follows:

1. Calculate the transition matrix from inertial frame to chaser's body frame, \mathbf{T}_I^B , using chaser's inertial attitude information;
2. Calculate the transition matrix from inertial frame to LVLH frame, $\mathbf{T}_I^{\text{LVLH}}$, using chaser's inertial position and inertial velocity information;
3. Calculate the transition from chaser's body frame to camera measure frame using camera installation information, i.e. camera offset \mathbf{r}_{cm}^B and orientation matrix \mathbf{T}_B^{CM} , by translation and rotation;

Finally, the relationship between vector in LVLH frame, \mathbf{x}_{LVLH} , and camera measure frame, \mathbf{x}_{CM} , is achieved as follows:

$$\mathbf{x}_{\text{CM}} = \mathbf{T}_B^{\text{CM}} \left[\mathbf{r}_{\text{cm}}^B + \mathbf{T}_I^B (\mathbf{T}_I^{\text{LVLH}})^{-1} \mathbf{x}_{\text{LVLH}} \right]. \quad (5)$$

The LOS measurement expressed in the LVLH frame is

$$\mathbf{Z} = \begin{bmatrix} \varepsilon \\ \theta \end{bmatrix} = \begin{bmatrix} \arctan\left(\frac{x\sqrt{x^2+y^2}+z(r_t-z)}{x(r_t-z)-z\sqrt{x^2+y^2}}\right) \\ \arctan\left(\frac{-y}{\sqrt{x^2+z^2}}\right) \end{bmatrix}, \quad (6)$$

where r_t is the average radius of debris circular motion. The measure sensitivity matrix \mathbf{H} can be further achieved by differentiating Eq. (6) with respect to relative state \mathbf{x} ; the Jacobian expression is as follows:

$$\mathbf{H} = \frac{\partial \mathbf{h}(\mathbf{x})}{\partial \mathbf{x}^T} = \begin{bmatrix} h_{11} & h_{12} & h_{13} & | & \mathbf{0}_{2 \times 3} \\ h_{21} & h_{22} & h_{23} \end{bmatrix}. \quad (7)$$

For specific expression of measure sensitivity matrix \mathbf{H} , please refer to Eq. (5) in [34].

To simplify the expression, the body frame of the chaser ($O_c - x_b y_b z_b$) is assumed to be aligned with measure frame (i.e. $\mathbf{r}_{cm} = \mathbf{0}$), and without loss of generality, the camera is assumed to be fixed along the x_b -axis of the chaser. Its characteristics needed for the derivation of the observability of the target are the full field of view (FOV), α , the minimal and maximal distance where the target is still identifiable, d_{min} and d_{max} , as well as the integration time needed to identify the target, Δt_r . The following tests need be executed for each detection step to check whether the target is observable, where l is the norm of \mathbf{l} :

1. $x_m > 0$, the target is in front of the chaser with respect to its x_m -axis;
2. $d_{min} < l < d_{max}$, the distance towards the target is within the given bounds;
3. $\left| \arctan\left(\frac{y_m}{x_m}\right) \right| < \frac{\alpha}{2}$, the target lies within the FOV in y_m direction;
4. $\left| \arctan\left(\frac{z_m}{x_m}\right) \right| < \frac{\alpha}{2}$, the target lies within the FOV in z_m direction.

Moreover, for the chaser to identify the target, the latter must continuously be observable during the timespan of Δt_r . Multiple entries and exits of the target from the FOV are permissible.

To calculate the attitude dynamics, the non-singular quaternion-based Euler's equations of motion were utilized:

$$\ddot{\mathbf{q}} = \frac{1}{2} \begin{bmatrix} 0 & -\mathbf{h}_0^T \\ \mathbf{h}_0 & -[\mathbf{h}_0] \times \end{bmatrix} \mathbf{q} + \frac{1}{2} \begin{bmatrix} 0 & -\boldsymbol{\omega}_b^T \\ \boldsymbol{\omega}_b & -[\boldsymbol{\omega}_b] \times \end{bmatrix} \dot{\mathbf{q}} + \begin{bmatrix} -\bar{\mathbf{q}}^T \\ q_0 \mathbf{I}_{3 \times 3} + [\bar{\mathbf{q}}] \times \end{bmatrix} \mathbf{J}^{-1} \mathbf{M}_c, \quad (8)$$

where $\mathbf{q} = [q_0 \ q_1 \ q_2 \ q_3]$ is the quaternion, $[\varepsilon] \times$ is a skew-symmetric cross-product matrix, \mathbf{J} is the inertia tensor of

chaser, \mathbf{M}_c is the external torque, $\bar{\mathbf{q}}$ is the vector part of \mathbf{q} , $\mathbf{I}_{3 \times 3}$ is the 3×3 unit diagonal matrix, $\boldsymbol{\omega}_b$ is the attitude angular velocity in body frame, and \mathbf{h}_0 can be calculated as follows:

$$\mathbf{h}_0 = -\mathbf{J}^{-1} [\boldsymbol{\omega}_b] \times \mathbf{J} \boldsymbol{\omega}_b. \quad (9)$$

Besides, $\boldsymbol{\omega}_b$ can be derived with quaternion \mathbf{q} and the quaternion rate $\dot{\mathbf{q}}$ as follows:

$$\boldsymbol{\omega}_b = 2 \begin{bmatrix} q_0 \dot{q}_1 - q_1 \dot{q}_0 + q_2 \dot{q}_3 - q_3 \dot{q}_2 \\ q_0 \dot{q}_2 - q_2 \dot{q}_0 + q_3 \dot{q}_1 - q_1 \dot{q}_3 \\ q_0 \dot{q}_3 - q_3 \dot{q}_0 + q_1 \dot{q}_2 - q_2 \dot{q}_1 \end{bmatrix}. \quad (10)$$

At long range, since stars remain visible in the field of view, the camera can deliver an attitude quaternion that helps to get rid of the camera bias alignment problem.

3 General Solution for Target Searching Problem

Given a measure of the uncertainty of the target's position and given certain an optical camera with limited detection capabilities, the following section will investigate possible search strategies for a target whose apparent motion is driven by orbital dynamics and inherent perturbations. A quantitative evaluation method is also proposed.

3.1 Outlier Detection

With finite probability, an initial state could be drawn that is very far away from the supposed state. For one-dimensional normal distributions, such outliers can easily be spotted by checking whether the drawn variable is outside a given metric, such as 3σ . However, for a multivariate, possibly correlated normal distribution the 3σ rule applied in each dimension would not sufficiently recognize outliers. A quantity that is able to handle multivariate, correlated normal distributions is the *Mahalanobis Distance*, Δ , defined as

$$\Delta^2 = (\mathbf{x} - \boldsymbol{\mu})^T \sum^{-1} (\mathbf{x} - \boldsymbol{\mu}) \quad (11)$$

which is a measure of how far away \mathbf{x} is from the center, taking into account the correlation. A constant Δ defines an ellipsoid of equal probability around the center. The value for Δ can be chosen via

$$P(\Delta < q_\beta) > \beta, \quad (12)$$

where β is the fraction of the total number of individuals that should lie within the ellipsoid.

3.2 Basic Discussion

In camera focal plane, we get the geometrical relationship between detection circle, A_{FOV} and targets relative position uncertainty ellipse, A_{Ellipse} . A_{Ellipse} is the projection of the ellipsoid on the focal plane. By control the relative motion between detection circle and ellipse, we can achieve the desired detection probability. Basically, there are two situations:

1. If $A_{\text{FOV}} \geq A_{\text{Ellipse}}$
When A_{Ellipse} totally lies inside A_{FOV} , the target will be detected 100% in probability; when A_{Ellipse} lies outside of A_{FOV} or just overlaps A_{FOV} in some part, rotate the camera to locate A_{Ellipse} inside of the detection circle, then the target also can be detected 100% in probability.
2. If $A_{\text{FOV}} < A_{\text{Ellipse}}$
First, point the camera/detection circle to some part of the ellipse; second, sweep the whole ellipse with a certain algorithm in limited time; the target will be detected in some probability.

3.3 Detection Efficiency Metrics

This paper's aim is to solve the single-optical camera based detection problem of non-cooperative space debris whose position is not known accurately (TLE-level precision). A way to assess the quality of the strategy found is first introduced. In order to evaluate the quality of the search strategy, each probable initial condition would have to be checked. Since this is not feasible, a Monte Carlo Simulation (MCS) approach is employed and Fig. 3 explains the methodology for MCS. Since perturbations and atmospheric drag are considered, it is not easy to analytically predict the motion of a target relative to the chaser. Thus, STK/HPOP is used to propagate the path of the target and the chaser. The main models are built in MATLAB, embedding STK API functions to run the high-fidelity orbit simulation.

4 Covariance Analysis-Based Searching Strategy

In order to tackle issues related to the difficulty of obtaining accurate and fast information on the position dispersion ellipsoid, i.e. the prediction of the relative position of the target while taking in account limited on-board processing resources we explore in the following chapter a solution based on linear covariance estimation.

4.1 Closed-Form Linear Covariance Analysis

The methodology is developed by applying linear covariance analysis techniques to a closed-loop guidance, navigation,

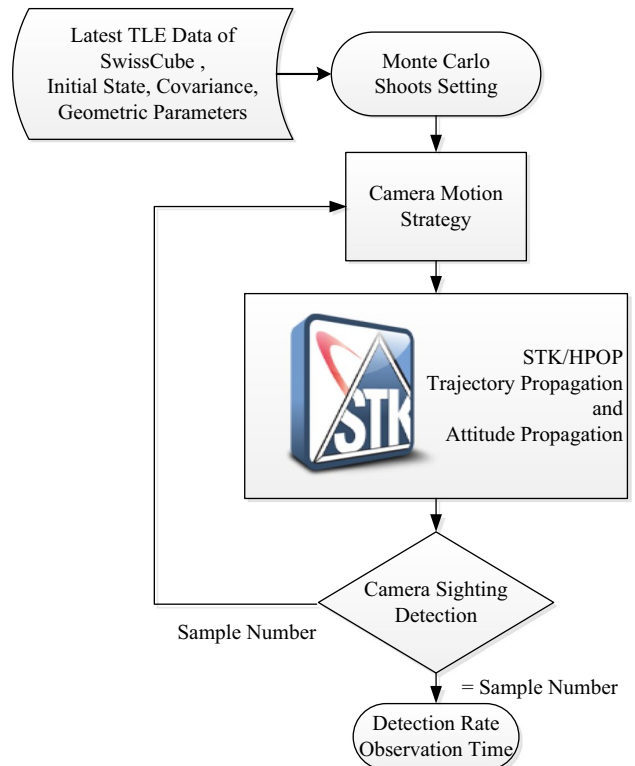


Fig. 3 Chart flow of target searching MCS

and control (GN&C) system [39–41] including the *orbit propagation*, *measurement update*, and *maneuver correction* steps. The methodology is designed to quickly and accurately predict the trajectory dispersions, navigation errors, and required maneuver at selected key points along a nominal trajectory, as described in Fig. 4.

Mathematically deduced as following: linearizing the true state \mathbf{x} and navigation state $\hat{\mathbf{x}}$ about the nominal trajectory defined by $\bar{\mathbf{x}}$, produces a set of equations that describe the time-evolution of state dispersions from the nominal, $\delta\mathbf{x} = \mathbf{x} - \bar{\mathbf{x}}$, and the time-evolution of navigation state dispersions, $\delta\hat{\mathbf{x}} = \hat{\mathbf{x}} - \bar{\mathbf{x}}$. We define an augmented error state vector \mathbf{X} consisting of the true dispersions and navigated dispersions

$$\mathbf{X} = \begin{bmatrix} \delta\mathbf{x} \\ \delta\hat{\mathbf{x}} \end{bmatrix}, \quad (13)$$

corresponding covariance of \mathbf{X} is $\mathbf{\Omega} = E[\mathbf{XX}^T]$. If the initial augmented state and covariance are \mathbf{X}_0 and $\mathbf{\Omega}_0$, respectively, each segment of the closed-loop GN&C process of AON-based autonomous rendezvous will be obtained as follows:

4.1.1 Orbit Propagation

$$\mathbf{X}_k^- = \Psi_{k|k-1} \mathbf{X}_{k-1}^+, \quad (14)$$

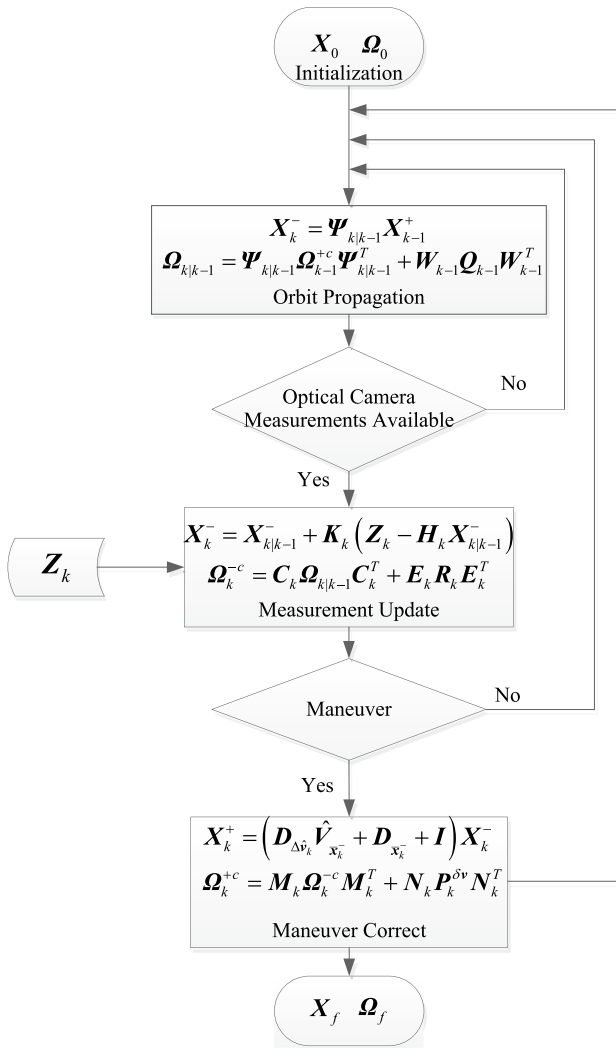


Fig. 4 Closed-form linear covariance analysis

$$\Omega_{k|k-1} = \Psi_{k|k-1} \Omega_{k|k-1}^{+c} \Psi_{k|k-1}^T + W_{k-1} Q_{k-1} W_{k-1}^T. \quad (15)$$

4.1.2 Measurement Update

$$\mathbf{X}_k^- = \mathbf{X}_{k|k-1}^- + \mathbf{K}_k (\mathbf{Z}_k - \mathbf{H}_k \mathbf{X}_{k|k-1}^-), \quad (16)$$

$$\mathbf{\Omega}_k^{-c} = \mathbf{C}_k \mathbf{\Omega}_{k|k-1}^{-c} \mathbf{C}_k^T + \mathbf{E}_k \mathbf{R}_k \mathbf{E}_k^T. \quad (17)$$

4.1.3 Maneuver Correcting

$$\mathbf{X}_k^+ = (D_{\Delta v_k} \hat{V}_{\bar{x}_k} + D_{\bar{x}_k} + I) \mathbf{X}_k^- \quad (18)$$

$$\mathbf{\Omega}_k^{+c} = \mathbf{M}_k \mathbf{\Omega}_k^{-c} \mathbf{M}_k^T + \mathbf{N}_k \mathbf{P}_k^{\delta v} \mathbf{N}_k^T. \quad (19)$$

For the specific expression of $\Psi_{k|k-1}$, W_{k-1} , Q_{k-1} , $\Omega_{k|k-1}$, \mathbf{K}_k , \mathbf{C}_k , \mathbf{E}_k , \mathbf{R}_k , $D_{\Delta v_k}$, $\hat{V}_{\bar{x}_k}$, $D_{\bar{x}_k}$, \mathbf{M}_k , \mathbf{N}_k , and $\mathbf{P}_k^{\delta v}$, please refer to “Appendix”.

4.2 Covariance-Based Searching Algorithm

Figure 5 shows the procedures of covariance-based target searching. Based on the current attitude and relative state, transfer the current covariance from LVLH to FOV, to calculate the relative geometry between ellipse and detection circle in focal plane, a specific algorithm is used to sweep the whole ellipse: use the sight model built in Sect. 2 to conduct target confirmation, considering constraints, such as detection time consumption, etc. If the target was not confirmed and the constraints keep satisfied, propagate the relative state and the covariance using *Closed-Loop Linear Covariance Tool*, propagate the attitude using *Quaternion-Based Euler's Equations*. Repeat the previous procedure until the target is found or out of constraints.

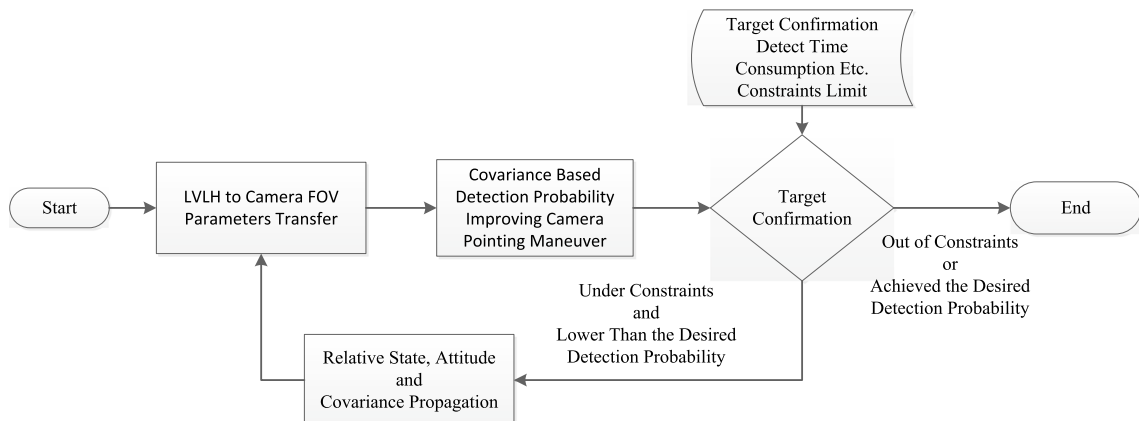


Fig. 5 Block diagram of covariance-based target searching strategy for lost in space

Based on the previous general idea, seven methods are developed, as follows:

4.2.1 Tracking Nominal Relative Trajectory

The camera is set to track along the nominal relative trajectory in FOV all the time.

4.2.2 Orbital Plane Sweeping

First, rotate the camera pointing to the nominal relative trajectory in FOV; second, rotate the camera in orbital plane about the normal direct y_m -axis back and forth, sweeping the dispersion ellipsoid,

$$\boldsymbol{\omega}_b(t) = \begin{bmatrix} 0 \\ \varepsilon_z(t) \frac{2\pi N}{t_D} \cos\left(\frac{2\pi N}{t_D} t\right) \\ 0 \end{bmatrix}, \quad (20)$$

where $\varepsilon_z(t) = \arctan(\sigma_z(t)/l(t))$ is the current desired rotation amplitude in rad, $\sigma_z(t)$ is the radial standard deviation, t_D is the total given detection time, N is the sweeping number.

4.2.3 Cross-Track Sweeping

Similarly as inside orbital sweeping, first, rotate the camera pointing to the nominal relative trajectory in FOV; second, rotate the camera in cross-track about the normal direct z_m -axis left and right, sweeping the dispersion ellipsoid,

$$\boldsymbol{\omega}_b(t) = \begin{bmatrix} 0 \\ 0 \\ \theta_y(t) \frac{2\pi N}{t_D} \cos\left(\frac{2\pi N}{t_D} t\right) \end{bmatrix}, \quad (21)$$

where $\theta_y(t) = \arctan(\sigma_y(t)/l(t))$ is the current desired rotation amplitude in rad, $\sigma_y(t)$ is the cross-track standard deviation, t_D and N as mentioned before.

4.2.4 Combined Sweeping

Similarly as inside and cross-track sweeping, first, rotate the camera pointing to the nominal relative trajectory in FOV; second, rotate the camera both in orbital plane and cross-track about the y_m -axis and z_m -axis, respectively. The attitude angular velocity in body frame is

$$\boldsymbol{\omega}_b(t) = \begin{bmatrix} 0 \\ \varepsilon_z(t) \frac{2\pi N_z}{t_D} \cos\left(\frac{2\pi N_z}{t_D} t\right) \\ \theta_y(t) \frac{2\pi N_y}{t_D} \cos\left(\frac{2\pi N_y}{t_D} t\right) \end{bmatrix}, \quad (22)$$

where N_z and N_y are the sweeping number of radial and normal direction, respectively. Other symbols are as previously described.

4.2.5 Eccentric Sweeping

Imitate the US Missile Early-Warning satellite scanning strategy: first, rotate the camera pointing to the nominal relative trajectory in FOV; second, generate an eccentric angle, $A_0 = \max(\varepsilon_z(t), \theta_y(t))$, about the line of sight, that is x_m -axis; finally, rotate the camera about the line of sight, and the attitude angular velocity in body frame is

$$\boldsymbol{\omega}_b(t) = \begin{bmatrix} A_0 + \frac{2\pi}{T_N} \left[\frac{t}{T_N} \right] \\ 0 \\ 0 \end{bmatrix}, \quad (23)$$

where T_N is the revolution about the x_m -axis; other symbols are as previously described.

4.2.6 Stepping Sweeping

In radial direction, the FOV center pointing along the radial diameter of ellipsoid steps upward from the bottom to the top; in the normal direction, the FOV sweeping the ellipsoid in a simple harmonic motion, and the attitude angular velocity in body frame is,

$$\boldsymbol{\omega}_b(t) = \begin{bmatrix} 0 \\ -\varepsilon_z(t) + \Delta_s \cdot \left[\frac{t}{T_N} \right] \\ \theta_y(t) \frac{2\pi N_y}{t_D} \sin\left(\frac{2\pi N_y}{t_D} t\right) \end{bmatrix}, \quad (24)$$

where $T_N = t_D/N_y$ is the revolution of normal harmonic motion, and other symbols are as previously described.

4.2.7 Double Harmonic Sweeping

The camera sweeps the dispersion ellipsoid in harmonic motion, both in radial and normal directions,

$$\boldsymbol{\omega}_b(t) = \begin{bmatrix} 0 \\ \varepsilon_z(t) \frac{2\pi N_z}{t_D} \cos\left(\frac{2\pi N_z}{t_D} t\right) \\ \theta_y(t) \frac{2\pi N_y}{t_D} \sin\left(\frac{2\pi N_y}{t_D} t\right) \end{bmatrix}, \quad (25)$$

where all symbols are as previously described.

4.3 Strategies Comparison

The SCB TLE from May 31, 2014 with epoch UTC 01:27:36 is chosen to serve as the predicted state. It was required that

Table 1 Target searching strategy performance comparison (STK/HPOP)

Strategy	$n_{loc/tot}$	n_{out}	$n_{loc/in}$	t_{max}/s	t_{avg}/s
Tracking nominal relative trajectory	974/1000 (97.40%)	1	973/999 (97.40%)	773	809 (80.85%)
Inside orbital sweeping	999/1000 (99.90%)	1	998/999 (99.90%)	103	379 (37.90%)
Cross-track sweeping	982/1000 (98.20%)	0	982/1000 (98.20%)	927	818 s (81.75%)
Combined sweeping	999/1000 (99.90%)	2	997/998 (99.90%)	302	318 s (31.80%)
Eccentric sweeping	991/1000 (99.10%)	1	990/999 (99.10%)	155	784 s (78.40%)
Stepping sweeping	1000/1000 (100.00%)	0	1000/1000 (100.00%)	236	40 (4.00%)
Double harmonic sweeping	996/1000 (99.60%)	0	996/1000 (99.60%)	995	77 (7.70%)

$n_{loc/tot}$ number of located individuals of all, n_{out} number of outliers, $n_{loc/in}$ number of located individuals of inliers, t_{max} longest time used of located individuals, t_{avg} average time recognizable of located individuals

Table 2 Target searching strategy performance comparison (J2 model)

Strategy	$n_{loc/tot}$	n_{out}	$n_{loc/in}$	t_{max}/s	t_{avg}/s
Tracking nominal relative trajectory	976/1000 (97.60%)	0	976/1000 (97.60%)	824	842 (84.15%)
Inside orbital sweeping	1000/1000 (100.00%)	1	999/999 (100.00%)	252	374 (37.40%)
Cross-track sweeping	982/1000 (98.20%)	0	982/1000 (98.20%)	660	822 (82.20%)
Combined sweeping	1000/1000 (100.00%)	1	999/999 (100.00%)	201	302 (30.15%)
Eccentric sweeping	993/1000 (99.30%)	1	992/999 (99.30%)	92	752 (75.20%)
Stepping sweeping	1000/1000 (100.00%)	0	1000/1000 (100.00%)	238	44 (4.40%)
Double harmonic sweeping	998/1000 (99.80%)	0	998/1000 (99.80%)	991	78 (7.80%)

99.9% of the individuals are to be spotted. Hence, for the given distribution Σ , the critical Mahalanobis distance is found to be $\Delta_C = q_{99.99\%} = 4.74$. Assuming that the sample is chosen to be at its highest probability, i.e. 0, in all but one direction, the sample would be considered an outlier, meaning $\Delta > \Delta_C$, if its absolute value in this direction was larger than the following values: $\Delta x = 2.164$ km, $\Delta y = 1.443$ km, $\Delta z = 4.673$ km, $\Delta \dot{x} = 5.812$ m/s, $\Delta \dot{y} = 2.621$ m/s, $\Delta \dot{z} = 3.824$ m/s.

Note that these values are considerably higher than three times the value of the square root of the diagonal values of Σ (i.e. 3σ). This is because the contours of the same probabilities are elongated in correlated distributions compared with non-correlated distributions, while the standard deviations remain the same. Hence if only the 3σ rule was considered, samples would be classified as outliers, although this is not the case in reality.

The structural parameters of chaser are consistent with [33]. Its camera is modeled to be fixed within the frame and look along the positive x_m -axis. The camera characteristics are chosen to be—if not stated otherwise—as $\alpha = 30^\circ \times 30^\circ$, $d_{min} = 0$ km, $d_{max} = 10$ km, and $\Delta t_r = 3$ s. The chaser is also propagated using HPOP, with the same force model applied to the target individuals. Its initial state and its orientation were dependent on the chosen strategy.

The nominal relative trajectory is a co-elliptical approaching trajectory, the initial relative state is

$\mathbf{x}_0 = [-6.0 \text{ km}, 0.0 \text{ km}, -4.0 \text{ km}, 6.3507 \text{ m/s}, 0.0 \text{ m/s}, 0.0 \text{ m/s}]^T$, the estimated residuals of SCB based on two periods TLE is Σ , Σ was evaluated with unit km for the position and unit m/s for the velocity residuals.

$$\Sigma_0 = \begin{bmatrix} 0.2437 & 0.1044 & 0.0387 & -0.0774 & -0.0954 & 0.0072 \\ 0.1044 & 1.5835 & 0.0198 & -1.1664 & -0.1080 & -0.0819 \\ 0.0387 & 0.0198 & 0.1062 & 0.0225 & -0.0567 & -0.0297 \\ -0.0774 & -1.1664 & 0.0225 & 2.3917 & 0.0738 & -0.0486 \\ -0.0954 & -0.1080 & -0.0567 & 0.0738 & 0.3634 & 0.0090 \\ 0.0072 & -0.0819 & -0.0297 & -0.0486 & 0.0090 & 0.6706 \end{bmatrix}.$$

The previous seven search strategies were tested in the MCS, with increasing attitude control complexity. The numbers of individuals drawn was 1000, if nothing else is mentioned. The given total detection time was set to be $t_D = 1000$ s. The computer used for simulation is Intel (R) Core (TM) i5-4260U CPU @ 1.40 GHz 2.00 GHz MacBook Air, installed with windows 64-bit system. Models are built with MATLAB R2013b and AGI\STK 9. Analysis results are shown in Table 1.

Using the accuracy HPOP model takes about 20 min to carry out the analysis for one strategy. In order to save time, we re-run the tests with a simplified orbit model, which is only considering the earth non-spherical gravity perturbation (J2 orbit model). The analysis time for

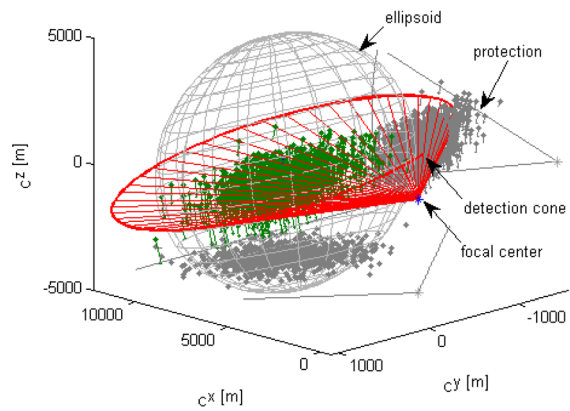
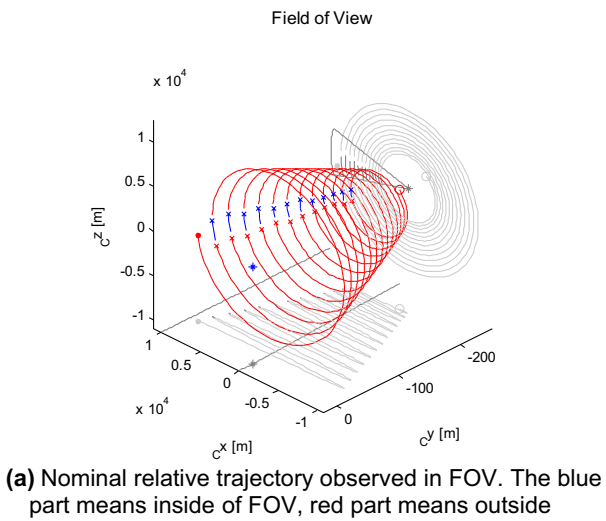


Fig. 6 Trajectories and initial population drawing using the Stepping Sweeping strategy, the simulated camera has a 30° FOV. **a** Nominal relative trajectory observed in FOV. The blue part means inside of FOV, red part means outside. **b** Initial positions of the individuals. Since the chaser rotates rapidly, the relative velocities of the individuals are high relative to camera frame

one strategy is reduced to one-tenth of the previous, about 2 min. The results are shown in Table 2.

Comparing the results presented in the two tables, the same strategy conducted under different orbit models yield very close detection results; therefore, considering the computational time reduction, the J2 orbit model will be used for the subsequent sensitivity analysis. For the target searching problem, we mainly care about the detection rate and the required search time; all the seven strategies can get a rather high detection rate, with the worst case (Tracking Nominal Rel. Traj.) yielding 97.4%. Excluding Cross-track sweeping, all the others achieved rates beyond 99%. Even though Combined Sweeping reached a 100% detection rate, Stepping

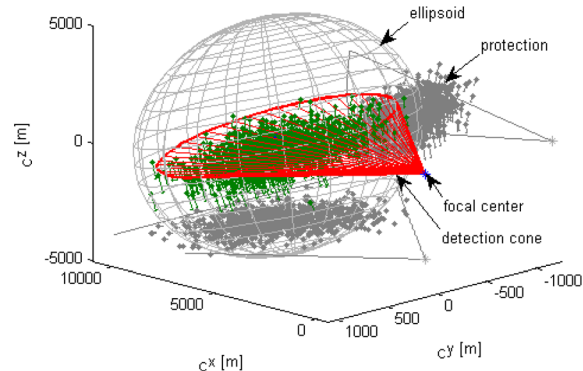
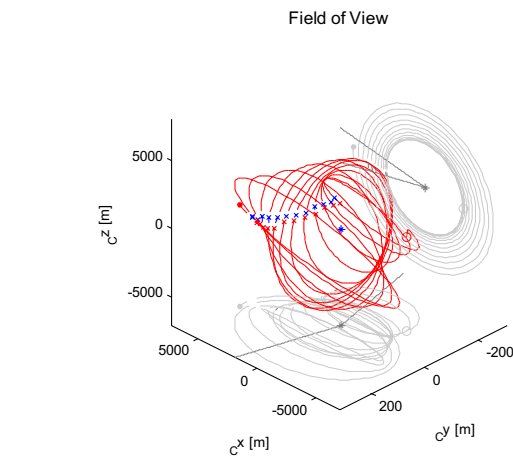


Fig. 7 Trajectories and initial population drawing using the Stepping Sweeping strategy, the simulated camera has a 19° FOV. **a** Nominal relative trajectory observed in FOV. The blue part means inside of FOV, red part means outside. **b** Initial positions of the individuals. Since the chaser rotates rapidly, the relative velocities of the individuals are high relative to camera frame

Sweeping was selected due to a significantly lower scanning time. The nominal relative trajectory and initial positions of individuals are shown in Fig. 6a, b.

In the previous case, at the beginning of search, the detection circle is bigger than the target's uncertainty ellipsoid in the normal direction, and an extra simulation with a narrower field of view camera, $\alpha = 19^\circ \times 19^\circ$ was also executed; other settings were kept the same. The nominal relative trajectory and initial positions of individuals are shown in Fig. 7a, b.

The simulation result is $n_{loc_in} = 1000/1000 (100.00\%)$, $n_{loc_in} = 998/998 (100.00\%)$, $n_{out} = 2$, $t_{max} = 882$ s, $t_{avg} = 17$ s (1.70%); although the detection rate maintains 100%, the

detection time consumption increases, from about 4 min to almost 15 min. This further proves the validity and robustness of the Stepping Sweeping strategy, which is applicable for general “lost in space” target detection problem. When the uncertainty is bigger, it certainly will take a longer time to accomplish the detection.

5 Sensitivity Analysis

In order to characterize the effect of camera parameters, a sensitivity analysis was carried out using the traversal method; the *Stepping Sweeping* strategy is employed for all the simulation cases. The parameters evaluated are those that affect mainly the camera such as *detecting range*, *aperture*, and *integration time*, as well as the mission conditions such as the *total detection duration* and the *nominal relative trajectory*.

5.1 Camera Parameters

Obviously, a stronger camera, which has longer detection range, bigger aperture, and shorter integration time, will make the target detected faster and succeed in higher probability.

5.1.1 Detection Range

We let the maximum distance (detection range) of the camera vary in $d_{max} = [7.5 \text{ km}, 12 \text{ km}]$ with a stepsize of 500 m; other parameters are kept the same as in Sect. 4. The changes of detection rate and required detection time vs camera detection range are shown in Fig. 8a, b.

It can be seen that below a certain threshold, detection rate starts dropping. This indicates that the camera system should be designed taking this feature into consideration in order to maximize mission success; knowing the initial relative state as well as covariance parameters, one should be able to estimate this value.

5.1.2 FOV

Let camera’s FOV α vary in $[15^\circ, 30^\circ]$ with a stepsize of 1° ; other parameters are kept the same as in Sect. 4. The changes of detection rate and scanning time consumption vs the camera’s FOV are shown in Fig. 9a, b.

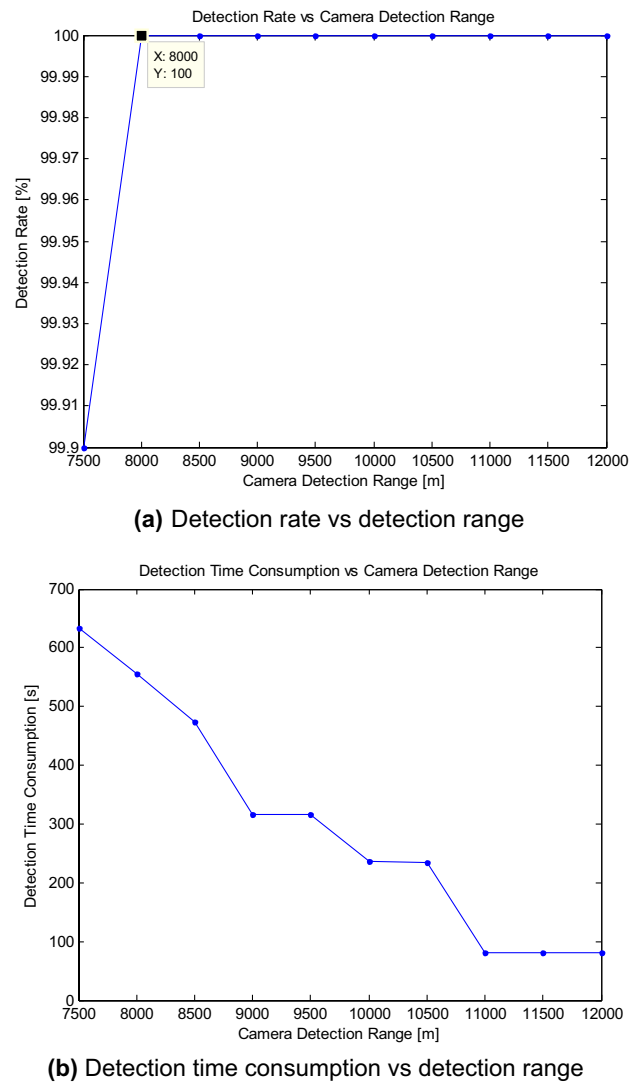


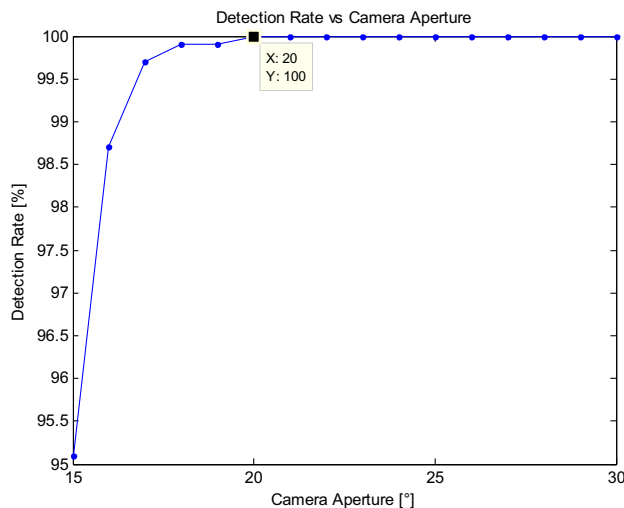
Fig. 8 Sensitivity analysis of the maximum detection range parameter. **a** Detection rate vs detection range. **b** Detection time consumption vs detection range

It reveals that a minimum FOV is needed to achieve the 100% detection rate; when the threshold is satisfied, the detection time consumption retains a stable value, this value is mainly determined by the searching algorithm, here take *Stepping Sweeping* strategy for example, the detection time consumption is between 4 and 5 min.

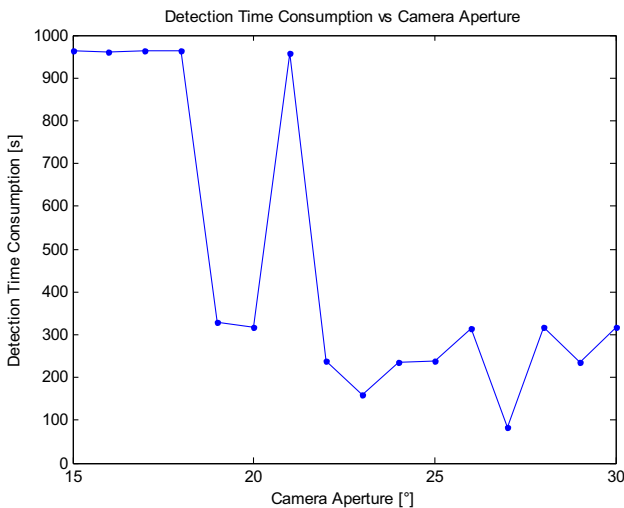
5.1.3 Acquisition Time/Integration Time

Let integration time Δt_r vary in [1 s, 10 s] with a stepsize of 1 s, other parameters are kept the same as in Sect. 4. The changes of detection rate and detection time consumption over acquisition time/integration time are shown in Fig. 10a, b.

In this situation we consider integration to mean the broader time to acquire and process one image since



(a) Detection rate vs camera FOV



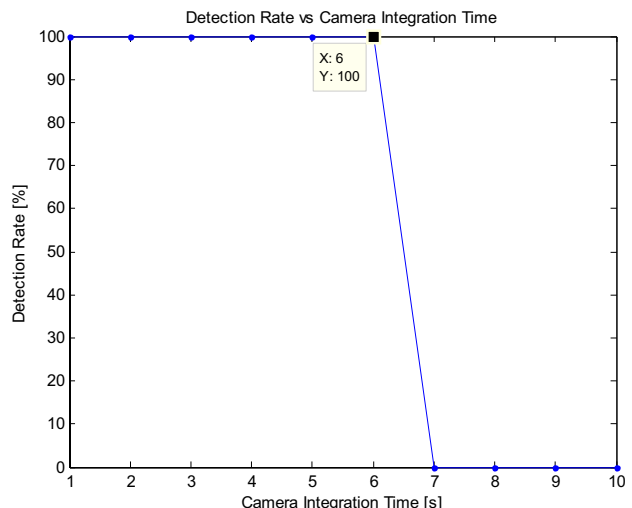
(b) Detection time consumption vs FOV.

Fig. 9 Sensitivity analysis of camera's FOV parameter. **a** Detection rate vs camera FOV. **b** Detection time consumption vs FOV

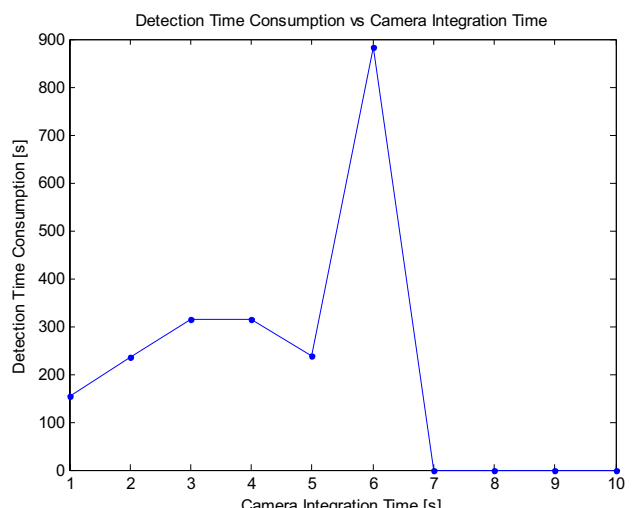
integration on the sensor itself depends on the lighting conditions, but typically requires less than 1 s.

5.2 Mission Condition

During the handover stage, stable relative navigation needs to be designed, in particular for angles-only navigation; the target should be first detected by the on-board relative measure sensor—optical camera. For safety reason, the *co-elliptical approaching* or *relative station keeping* trajectory is commonly used; for lighting and telemetry communication requirements, the target should be searched as soon as possible. In this subsection, we will quantitatively analyze these mission conditions' influence on target search.



(a) Detection rate vs integration time



(b) Detection time consumption vs integration time

Fig. 10 Sensitivity analysis of camera's acquisition time parameter. **a** Detection rate vs integration time. **b** Detection time consumption vs integration time

5.2.1 Allowed Search Duration

Let the allowed search duration (detection duration) t_D vary in $[10 \text{ s}, 1000 \text{ s}]$ with a stepsize of 10 s, other parameters are kept the same as in Sect. 4. The related changes of detection rate and detection time consumption over total detection duration are shown in Fig. 11a, b.

In Fig. 11a, it can be seen that when the time allotted for scanning the surroundings for the target is longer than 230 s, a stable 100% detection rate can be achieved. Indeed,

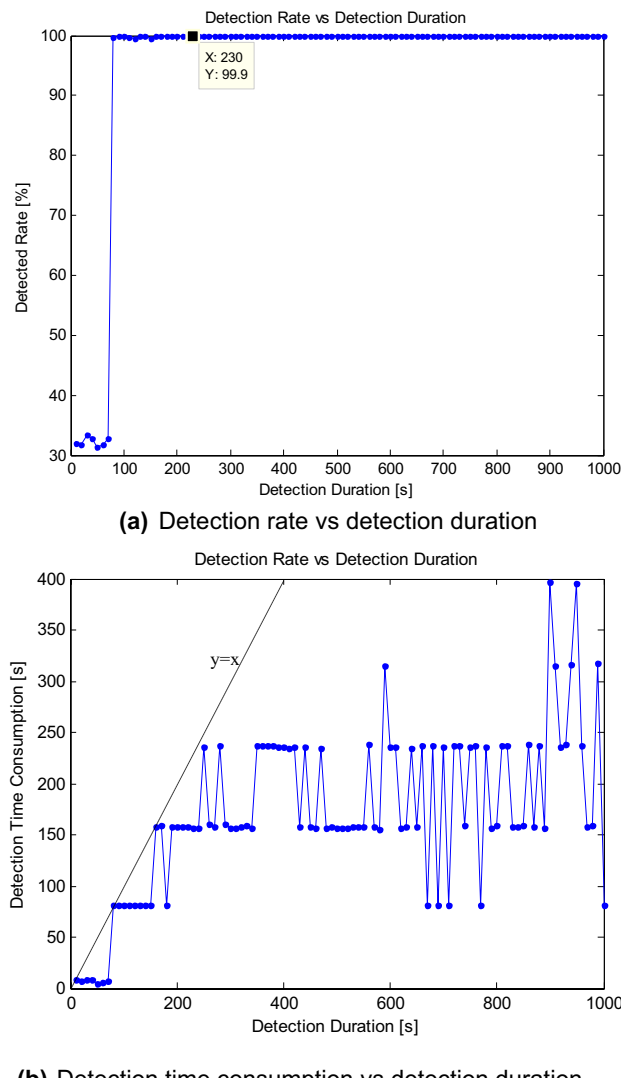


Fig. 11 Sensitivity analysis of allowed search duration. **a** Detection rate vs detection duration. **b** Detection time consumption vs detection duration

when looking at Fig. 11b, the detection time consumption curve starts to deviate from the $y=x$ line which indicates that given the current parameters, the search for the target seldom requires more than 230 s.

Table 3 Detection performance compared with different nominal relative trajectories (J2 model)

Strategy	$n_{\text{loc}}/\text{tot}$	n_{out}	n_{loc}/in	t_{\max}/s	t_{avg}/s
Tracking nominal relative trajectory	1000/1000 (100.00%)	0	1000/1000 (100.00%)	238	44 (4.40%)
Inside orbital sweeping	1000/1000 (100.00%)	0	1000/1000 (100.00%)	235	44 (4.40%)
Cross-track sweeping	1000/1000 (100.00%)	1	999/999 (100.00%)	81	43 (4.30%)
Combined sweeping	1000/1000 (100.00%)	1	999/999 (100.00%)	643	31 (3.10%)
Eccentric sweeping	1000/1000 (100.00%)	2	998/998 (100.00%)	61	31 (3.10%)
Stepping sweeping	1000/1000 (100.00%)	1	999/999 (100.00%)	581	31 (3.10%)

5.2.2 Nominal Relative Trajectory

Six common relative trajectories used for the handover between absolute navigation and relative navigation are evaluated with the results presented in Table 3.

In “relative station keeping”, the chaser will stay in a fixed position ahead/behind relative to the target. Using a “two-impulse rendezvous”, the chaser will burn twice, once at the beginning and once more at the end of a given time interval (set to 3000 s) to accomplish the transfer between initial and desired relative states. Here the initial relative state is set to 6 km behind and 4 km below, i.e. $\mathbf{x}_0 = [-6.0 \text{ km}, -4.0 \text{ km}, 0.0 \text{ km}, 0.0 \text{ m/s}, 0.0 \text{ m/s}, 0.0 \text{ m/s}]^T$, and final relative state to 2 km behind, i.e. $\mathbf{x}_f = [-2.0 \text{ km}, 0.0 \text{ km}, 0.0 \text{ km}, 0.0 \text{ m/s}, 0.0 \text{ m/s}, 0.0 \text{ m/s}]^T$. Based on the Hill guidance law, the two maneuver impulses are calculated, i.e. $\Delta \mathbf{v}_0 = [1.07 \text{ m/s}, 0.0 \text{ m/s}, -1.40 \text{ m/s}]^T$ and $\Delta \mathbf{v}_f = [1.05 \text{ m/s}, 0.0 \text{ m/s}, -1.47 \text{ m/s}]^T$.

A “fly around” configuration will have the chaser circumnavigate the target, which is colocated at the center of an ellipse trajectory whose semi-major axis (6 km) is along x -axis and the semi-minor axis (3 km) along z -axis.

In a “slow cross track maneuver”, the chaser would oscillate in cross-track, decoupled with the in orbital motion; here set it oscillates at the – 6 km relative station keeping point.

Finally, in “ v -bar hopping” the chaser will “hop” radially inside of orbit plane (along the x -axis). In all three trajectories, the period equals that of the orbital period.

Simulation results show that the strategy is applicable to all the common relative trajectories; however, each with specific advantages. If “slow cross track maneuver” or “two-impulse rendezvous” is used, the detection time is much shorter, but more fuel is needed. In the presence of large uncertainties in the along-track separation and radial, such as with TLE precision target location and angles-only navigation, finding the target within several minutes is safe enough from the point of view of safety and fuel saving. As a baseline, it would be recommended to choose the slower *co-elliptical approaching* or *relative station keeping* trajectory as the nominal relative trajectory for target search.

6 Conclusion

Inspired by “lost in space” target searching problem for single-camera based micro-/nano-satellite ADR, this paper employed the linear covariance techniques to direct on-board camera pointing control profile design, using Clohessy–Wiltshire dynamics as a base. A closed-loop linear covariance framework for AON was designed to evaluate seven target searching algorithms. In order to conduct the strategy performance comparison as well as sensitivity analysis, a STK/HPOP embedded MCS tool was built; all the MCS were conducted using this tool.

The results let appear that three strategies, *Inside Orbital Sweeping*, *Combined Sweeping*, and *Stepping Sweeping* offer the best results, with detection rates of nearly 100%. More specifically, the *Stepping Sweeping* strategy is shown to be robust against target’s position uncertainty and is applicable to all the common relative trajectories in orbital proximity operations presented in Sect. 5. Those results can also be used to determine required optical performances of camera and mission through the STK/HPOP embedded MCS tool.

The idea presented in this paper is an initial solution for “lost in space” of single-camera based nanosatellite ADR, as the closed-loop linear covariance analysis-based target searching method remains non-trivial from a computational resources point-of-view. Provided it can be adapted for space-bound hardware it could provide an interesting solution to the problem of handing over navigation control from on-ground to on-board hardware. Further works should focus on integrating further sensor information such as MEMS IMU measurements for instance.

Acknowledgements The authors acknowledge financial support from the China Scholarship Council (number 201, 403, 160, 417), Space Engineering Center of École Polytechnique Fédérale de Lausanne, and the National Natural Science Foundation of China (number 11572345 and 11222215). The authors would like to thank the editor and the anonymous reviewers for their constructive comments.

Appendix: Angles-Only Navigation Closed-Form Linear Covariance Analysis

In Eq. (14) $\Psi_{k|k-1}$ is the augmented state transfer matrix, its expression is

$$\Psi_{k|k-1} = \begin{bmatrix} \Phi(t_k, t_{k+1}) & \mathbf{0}_{6 \times 6} \\ \mathbf{0}_{6 \times 6} & \Phi(t_k, t_{k+1}) \end{bmatrix}. \quad (26)$$

In Eq. (15) \mathbf{Q}_{k-1} is the system noise matrix,

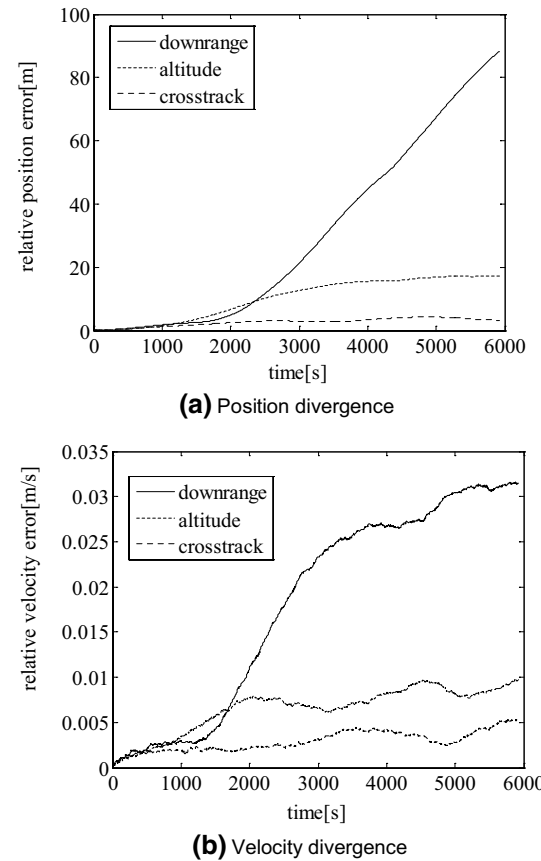


Fig. 12 Relative state divergence. **a** Position divergence. **b** Velocity divergence

$$\mathbf{Q}_{k-1} = \sigma_{\text{system_noise}} \cdot \begin{bmatrix} \Delta_t^3/3 & 0 & 0 & \Delta_t^2/2 & 0 & 0 \\ 0 & \Delta_t^3/3 & 0 & 0 & \Delta_t^2/2 & 0 \\ 0 & 0 & \Delta_t^3/3 & 0 & 0 & \Delta_t^2/2 \\ \Delta_t^2/2 & 0 & 0 & \Delta_t & 0 & 0 \\ 0 & \Delta_t^2/2 & 0 & 0 & \Delta_t & 0 \\ 0 & 0 & \Delta_t^2/2 & 0 & 0 & \Delta_t \end{bmatrix}, \quad (27)$$

where $\sigma_{\text{system_noise}} = (1 \times 10^{-4})^2$, Δ_t is the simulation time step size; if $\Delta_t = 1$ s, in one orbital period the position divergence is about 100 m, velocity divergence is about 0.03 m/s compared with the STK/HPOP: the relative state divergence figures vary with time are shown in Fig. 12.

In Eq. (15) \mathbf{W}_{k-1} is the system noise transfer matrix, its expression is

$$\mathbf{W}_{k-1} = \begin{bmatrix} \mathbf{I}_{6 \times 6} \\ \mathbf{0}_{6 \times 6} \end{bmatrix}. \quad (28)$$

In Eq. (14) $\Omega_{k|k-1}$ is the augmented state covariance, its initial value Ω_0 is

$$\Omega_0 = \begin{bmatrix} \mathbf{P}_0 & \mathbf{0}_{6 \times 6} \\ \mathbf{0}_{6 \times 6} & \hat{\mathbf{P}}_0 \end{bmatrix}, \quad (29)$$

where \mathbf{P}_0 is the priori real relative state covariance, $\hat{\mathbf{P}}_0$ is the priori estimated relative state covariance.

In Eq. (16) \mathbf{K}_k is Kaman Filter gain matrix, whose expression is

$$\mathbf{K}_k = \hat{\mathbf{P}}_{k|k-1} \mathbf{H}_k^T \left(\mathbf{H}_k \hat{\mathbf{P}}_{k|k-1} \mathbf{H}_k^T + \mathbf{R}_k \right)^{-1}. \quad (30)$$

In Eq. (17) \mathbf{R}_k is the measure noise matrix, whose expression is

$$\mathbf{R}_k = \begin{bmatrix} \sigma_\epsilon^2 & 0 \\ 0 & \sigma_\theta^2 \end{bmatrix}, \quad (31)$$

where σ_ϵ^2 and σ_θ^2 are the standard deviation of elevation and azimuth measurement.

The expression of \mathbf{E}_k is

$$\mathbf{E}_k = \begin{bmatrix} \mathbf{0}_{6 \times 2} \\ \mathbf{K}_k \end{bmatrix}. \quad (32)$$

The expression of \mathbf{C}_k is

$$\mathbf{C}_k = \begin{bmatrix} \mathbf{I}_{6 \times 6} & \mathbf{0}_{6 \times 6} \\ \mathbf{K}_k \mathbf{H}_k & \mathbf{I}_{6 \times 6} - \mathbf{K}_k \mathbf{H}_k \end{bmatrix}. \quad (33)$$

Assume at time t_k , the chaser need to execute an impulsive maneuver, the current estimated relative state is $\hat{\mathbf{x}}_k = [\hat{\mathbf{r}}_k^T \hat{\mathbf{v}}_k^T]^T$, the targeting final relative state is $\hat{\mathbf{x}}_f = [\hat{\mathbf{r}}_f^T \hat{\mathbf{v}}_f^T]^T$; employing the Hill guidance law to calculate the maneuver vector, it is

$$\Delta\hat{\mathbf{v}}_k = \Phi_{rv}^{-1}(t_f, t_k) [\mathbf{r}_f - \Phi_{rr}(t_f, t_k) \hat{\mathbf{r}}_k] - \hat{\mathbf{v}}_k. \quad (34)$$

So, $\hat{\mathbf{V}}_{\bar{\mathbf{x}}_k^-}$ in Eq. (18) as

$$\begin{aligned} \hat{\mathbf{V}}_{\bar{\mathbf{x}}_k^-} &= \frac{\partial \Delta\hat{\mathbf{v}}_k}{\partial \mathbf{x}} \Big|_{\bar{\mathbf{x}}_k^-} \\ &= [-\Phi_{rv}^{-1}(t_f, t_k) \Phi_{rr}(t_f, t_k) \mathbf{I}_{3 \times 3}]. \end{aligned} \quad (35)$$

As the impulsive maneuver is assumed, during the maneuver no position change will occur, that is

$$\mathbf{d}(\hat{\mathbf{x}}_k, \Delta\hat{\mathbf{v}}_k, t_k) = \begin{bmatrix} \mathbf{0}_{3 \times 1} \\ \Delta\hat{\mathbf{v}}_k + \Delta\mathbf{w}_k \end{bmatrix}. \quad (36)$$

So, $\mathbf{D}_{\Delta\hat{\mathbf{v}}_k}$ can be achieved by

$$\mathbf{D}_{\Delta\hat{\mathbf{v}}_k} = \frac{\partial \mathbf{d}(\hat{\mathbf{x}}_k, \Delta\hat{\mathbf{v}}_k, t_k)}{\partial \Delta\hat{\mathbf{v}}_k} \Big|_{\bar{\mathbf{x}}_k^-} = \begin{bmatrix} \mathbf{0}_{3 \times 1} \\ \mathbf{I}_{3 \times 1} \end{bmatrix}. \quad (37)$$

$\mathbf{D}_{\bar{\mathbf{x}}_k^-}$ can be achieved by

$$\mathbf{D}_{\bar{\mathbf{x}}_k^-} = \frac{\partial \mathbf{d}(\hat{\mathbf{x}}_k, \Delta\hat{\mathbf{v}}_k, t_k)}{\partial \mathbf{x}} \Big|_{\bar{\mathbf{x}}_k^-} = \begin{bmatrix} \mathbf{0}_{3 \times 1} \\ \mathbf{0}_{3 \times 1} \end{bmatrix}. \quad (38)$$

The expression of \mathbf{M}_k is

$$\mathbf{M}_k = \begin{bmatrix} \mathbf{D}_{\bar{\mathbf{x}}_k^-} + \mathbf{I}_{6 \times 6} & \mathbf{D}_{\Delta\hat{\mathbf{v}}_k} \hat{\mathbf{V}}_{\bar{\mathbf{x}}_k^-} \\ \mathbf{0}_{6 \times 6} & \mathbf{D}_{\Delta\hat{\mathbf{v}}_k} \hat{\mathbf{V}}_{\bar{\mathbf{x}}_k^-} + \mathbf{D}_{\bar{\mathbf{x}}_k^-} + \mathbf{I}_{6 \times 6} \end{bmatrix}. \quad (39)$$

The expression of \mathbf{N}_k is

$$\mathbf{N}_k = \begin{bmatrix} \mathbf{I}_{6 \times 6} \\ \mathbf{0}_{6 \times 6} \end{bmatrix}. \quad (40)$$

In Eq. (19) $\mathbf{P}_k^{\delta\mathbf{v}}$ is the control error covariance,

$$\mathbf{P}_k^{\delta\mathbf{v}} = \begin{bmatrix} \sigma_{vx}^2 & 0 & 0 \\ 0 & \sigma_{vy}^2 & 0 \\ 0 & 0 & \sigma_{vz}^2 \end{bmatrix}, \quad (41)$$

where σ_{vx}^2 , σ_{vy}^2 , and σ_{vz}^2 are the standard deviations of maneuver execution along three axis.

References

- Wormnes K, Le Letty R, Summerer L, Schonenborg R, Dubois-Matra O, Luraschi E et al (2013) ESA technologies for space debris remediation. In: Proceedings of the 6th IAASS conference: safety is not an option, Apr. 2013, pp 3–4
- Esmiller B, Jacqueland C, Eckel HA, Wnuk E (2014) Space debris removal by ground-based lasers: main conclusions of the European project CLEANSPACE. Appl Opt 53(31):145–154
- Lee SC, Kim HD, Suk J (2012) Collision avoidance maneuver planning using GA for LEO and GEO satellite maintained in keeping area. Int J Aeronaut Space Sci 13(4):474–483
- Pelton JN (2015) Current space debris remediation and on-orbit servicing initiatives. New solutions for the space debris problem. Springer International Publishing, Cham, pp 11–29
- Geller D (2007) Analysis of the relative attitude estimation and control problem for satellite inspection and orbital rendezvous. J Aeronaut Sci 55(2):195–214
- Woffinden DC, Geller DK (2009) Optimal orbital rendezvous maneuvering for angles-only navigation. J Guidance Control Dyn 32(4):1382–1387
- Woffinden DC, Geller DK (2009) Observability criteria for angles-only navigation. Aerosp Electron Syst IEEE Trans 45(3):1194–1208
- Li JR, Li HY, Tang GJ, Luo YZ (2011) Research on the strategy of angles-only relative navigation for autonomous rendezvous. Sci China Technol Sci 54(7):1865–1872
- Tombasco J, Axelrad P (2012) Along-track separation uncertainty modeling given space-based optical observations. J Guidance Control Dyn 35(3):732–739
- D'Amico S, Ardaens JS, Gaias G, Benninghoff H, Schlepp B, Jørgensen JL (2013) Noncooperative rendezvous using angles-only

- optical navigation: system design and flight results. *J Guidance Control Dyn* 36(6):1576–1595
11. Grzymisch J, Fichter W (2014) Observability criteria and unobservable maneuvers for in-orbit bearings-only navigation. *J Guidance Control Dyn* 37(4):1250–1259
 12. LeGrand KA, DeMars KJ, Pernicka HJ (2015) Bearings-only initial relative orbit determination. *J Guidance Control Dyn* 38(9):1699–1713
 13. Geller DK, Perez A (2015) Initial relative orbit determination for close-in proximity operations. *J Guidance Control Dyn* 38(9):1833–1841
 14. Klein I, Geller DK (2015) Zero delta-V solution to the angles-only range observability problem during orbital proximity operations. In: Choukroun D, Oshman Y, Thienel J, Idan M (eds) Advances in estimation, navigation, and spacecraft control. Springer, Berlin, pp 351–369
 15. Woffinden DC (2008) Angles-only navigation for autonomous orbital rendezvous. ProQuest, 2008
 16. Schmidt J, Lovell TA (2008) Estimating geometric aspects of relative satellite motion using angles-only measurements. In: Proceedings of AIAA/AAS astrodynamics specialist conference and exhibit, Honolulu, Hawaii, 2008
 17. Allen AC, Langley C, Mukherji R, Taylor AB, Umasuthan M, Barfoot TD (2008) Rendezvous lidar sensor system for terminal rendezvous, capture, and berthing to the international space station. In: SPIE defense and security symposium, international society for optics and photonics, 2008
 18. Zimpfer D, Kachmar P, Tuohy S (2005) Autonomous rendezvous, capture and in-space assembly: past, present and future. In: 1st Space exploration conference: continuing the voyage of discovery, Orlando, Florida, USA, vol 1, Jan. 2005, pp 234–245
 19. Rumford TE (2003) Demonstration of autonomous rendezvous technology (DART) project summary. In: AeroSense 2003, international society for optics and photonics, 2003
 20. Weismuller T, Leinz M (2006) GN&C technology demonstrated by the orbital express autonomous rendezvous and capture sensor system. In: 29th Annual AAS guidance and control conference, Feb. 2006, pp 06–016
 21. Carpenter JR (2011) A summary of the rendezvous, proximity operations, docking, and undocking (RPODU) lessons learned from the defense advanced research project agency (DARPA) orbital express (OE) demonstration system mission. NASA TM-2011-217088, 2011
 22. Bodin P, Noteborn R, Larsson R, Karlsson T, D'Amico S, Ardaens JS, Berges JC (2012) The prisma formation flying demonstrator: overview and conclusions from the nominal mission. *Adv Astronaut Sci* 144:441–460
 23. Noteborn R, Bodin P, Larsson R, Chasset C (2011) Flight results from the PRISMA optical line of sight based autonomous rendezvous experiment. In: 4th International conference on spacecraft formation flying missions and technologies, St-Hubert, Canada, 2011
 24. Delpech M, Berges J-C, Karlsson T, Malbet F (2013) Results of PRISMA/FFIORD extended mission and applicability to future formation flying and active debris removal missions. *Int J Space Sci Eng* 1(4):382–409
 25. Thevenet JB (2008) A generic radio-frequency subsystem for high altitude formation flying missions. In: Proceedings of the 3rd international symposium on formation flying missions and technologies, Noordwijk, The Netherlands, 2008
 26. Jørgensen JL, Denver T, Jørgensen PS (2004) Using an autonomous star tracker as formation flying sensor. *Small Satell Syst Serv* 571:1–5
 27. Wanqing X, Liying T, Jing M, Yang L (2011) Received power attenuation analysis based on wavelet for reflection-style optical antenna deformations in free-space laser communications. *Int J Antennas Propag.* <https://doi.org/10.1155/2011/614536>
 28. Zhou YP, Fu S, Yu SY et al (2010) Acquisition-probability model of nocooperative maneuvering target detection in space. *Infrared Laser Eng* 39(4):639–643
 29. Jono T, Toyoda M, Nakagawa K et al (1999) Acquisition, tracking and pointing system of OICETS for flee space laser communications. *SPIE* 3692:41–50
 30. Bismoot A, Zaltzman A, Arnon S (2001) Novel method for acquisition and identification of satellites in a cluster for laser communication application. *SPIE* 4489:215–221
 31. Feng GZ, Yang HJ, Qiu Q et al (2010) Analyzing from simulation of optimizing the spiral scan in the laser radar system. *Infrared Laser Eng* 35(2):165–168
 32. Yu SY, Gao HD, Ma J et al (2002) Selection of acquisition scan methods in intersatellites optical communications. *Chin J Lasers B* 11(5):364–368
 33. Stefan JF (2014) Lost in space. Master dissertation, Space Engineering Center, École Polytechnique Fédérale de Lausanne, Lausanne, Switzerland, 2014
 34. You Y, Wang H, Paccolat C et al (2017) Time and covariance threshold triggered optimal uncooperative rendezvous using angles-only navigation. *Int J Aerosp Eng* 5451908:1–10
 35. You Y, Wang H, Tang GJ et al (2016) Simulation toolkit for onboard optimal maneuver planning in active debris removal using angles-only navigation. In: 2016 3rd International conference on information and communication technology for education (ICTE 2016), ISBN: 978-1-60595-372-4, Toronto, Canada, Aug. 02–03, 2016
 36. You Y, Wang H, Paccolat C et al (2016) Square root unscented Kalman filter-based angles-only relative navigation using camera offset. *J Astronaut* 37(11):1312–1322 (**in Chinese**)
 37. You Y, Wang H, Paccolat C et al (2017) Closed-loop covariance analysis for orbital rendezvous using square root UKF based angles-only navigation. *J Natl Univ Def Technol* 39(4):33–39 (**in Chinese**)
 38. Fehse W (2003) Automated rendezvous and docking of spacecraft. Cambridge Univ Press, Cambridge, pp 424–440
 39. Geller DK (2006) Linear covariance techniques for orbital rendezvous analysis and autonomous onboard mission planning. *J Guidance Control Dyn* 29(6):1404–1414
 40. Li JR, Li HY, Tang GJ (2011) Optimal multi-objective trajectory design based on close-looped control for autonomous rendezvous. *Sci China Technol Sci* 54(11):3091–3097
 41. de Mijolla L, Cavrois B, Profizi A, Renault C, Cropp A (2013) Covariance analysis tool for far non-cooperative rendezvous. In: AIAA Guidance, Navigation, and Control Conference, AIAA, Boston, MA, 2013, pp 1–16

Publisher's Note Springer Nature remains neutral with regard to jurisdictional claims in published maps and institutional affiliations.